# Hot-hole transport and noise phenomena in silicon at cryogenic temperatures from first principles

David S. Catherall and Austin J. Minnich [*]

*Division of Engineering and Applied Science, California Institute of Technology, Pasadena, California 91125, USA*

(Received 28 June 2023; accepted 21 November 2023; published 19 December 2023)

The transport properties of hot holes in silicon at cryogenic temperatures exhibit several anomalous features, including the emergence of two distinct saturated drift velocity regimes and a nonmonotonic trend of the current noise versus electric field at microwave frequencies. Despite prior investigations, these features lack generally accepted explanations. Here, we examine the microscopic origin of these phenomena by extending a recently developed *ab initio* theory of high-field transport and noise in semiconductors. We find that the drift velocity anomaly may be attributed to scattering dominated by acoustic phonon emission, leading to an additional regime of drift velocity saturation at temperatures ~40 K for which the acoustic phonon occupation is negligible; while the nonmonotonic trend in the current noise arises due to the decrease in momentum relaxation time with electric field. The former conclusion is consistent with the findings of prior work, but the latter distinctly differs from previous explanations. This work highlights the use of high-field transport and noise phenomena as sensitive probes of microscopic charge transport phenomena in semiconductors.

DOI: 10.1103/PhysRevB.108.235207

## I. INTRODUCTION

The microscopic processes underlying charge transport in semiconductors are of fundamental and practical interest [1–5]. Numerical approaches to study transport phenomena have typically employed Monte Carlo simulations [1], which are capable of treating realistic device geometries [6,7] and have been extended to full-band simulators [8,9]. Within the last decade, the development of the *ab initio* treatment of the electron-phonon interaction has enabled the calculation of transport properties in homogeneous systems without any fitting parameters [4,5]. Recent findings with these methods include the importance of two-phonon scattering in GaAs [10,11] and Si [12] as well as the discovery of simultaneously high electron and hole mobilities in BAs [13–15]. Most *ab initio* calculations have been restricted to the low-field regime in which electrons are in thermal equilibrium with the lattice. However, outside of the low-field regime, phenomena such as field-dependent mobility, drift velocity saturation, and negative differential resistance may occur [16–18]. Furthermore, at high fields qualitatively new information can be obtained from noise quantities, such as the current fluctuation power spectral density (PSD), due to the breakdown of equilibrium relationships including the Einstein [19] and Nyquist equations [20]. Recent studies have extended the *ab initio* method to the high-field regime and applied them to both transport and noise in GaAs [11,21] and Si [12,22].

Charge transport in *p*-Si at cryogenic temperatures and microwave frequencies is of particular interest due to two anomalous transport characteristics. First, at large electric fields of tens of $\mathrm{kVcm^{-1}}$, semiconductors generally exhibit drift velocity saturation in which the drift velocity no longer increases with field [1]. In *p*-Si below 40 K, an additional regime of drift velocity saturation occurs at considerably smaller fields, approximately 0.1 $\mathrm{kVcm^{-1}}$ [17]. This feature has been studied numerically by semianalytical [23,24] and full-band Monte Carlo methods [25]. While an initial investigation attributed the feature to the nonparabolic hole dispersion and Bose-Einstein distribution occupation of phonons [23], a later study instead attributed the behavior solely to population of the spin-orbit band at high fields [24]. The "shoulder" feature has more recently been computationally reproduced using full-band Monte Carlo [25], but without analysis. Therefore, the explanation of the anomalous saturation regime remains unresolved.

A second anomalous feature appears in the PSD. It has been observed experimentally that in *p*-Si at 10 GHz and 77 K, a nonmonotonic (peak) trend with increasing dc electric field is observed for current noise both longitudinal and transverse to the field. This feature has also been observed in *n*-Si and Ge [26,27]. The trend was originally ascribed to an initial increase due to carrier heating followed by a decrease due to a decreasing momentum relaxation time at high fields [27]. In Sec. 9.3 of Ref. [28], the trend was attributed to a field-dependent energy relaxation time which influences the convective noise mechanism (described in Sec. 7.2 of the same reference). The convective mechanism arises from the coupling of velocity and energy fluctuations of the charge carriers, leading to a decrease in the PSD with increasing electric field for materials with a sublinear current-voltage characteristic. Given these differing explanations, the origin of the peak remains unclear.

Here, we investigate these phenomena by computing the drift velocity and PSD versus field of hot holes in silicon between 6 and 77 K using a modified implementation of the high-field *ab initio* method which is applicable at cryogenic temperatures. We show that the additional drift velocity saturation regime arises from scattering dominated by acoustic

[*]aminnich@caltech.edu

 ©2023 American Physical Society

phonon emission. For the PSD, we find that the peak occurs due to the decrease of the momentum relaxation time with increasing electric field, an explanation not given in prior literature. This work demonstrates the use of high-field first-principles transport and noise calculations as useful tools in investigating the microscopic phenomena in charge transport.

## II. THEORY AND NUMERICAL METHODS

### A. Overview

The methods used in this work have been described previously [11,21,22]. Briefly, the transport of charge carriers due to an applied electric field may be described by the Boltzmann transport equation (BTE). For a spatially homogeneous system, the BTE is given by

$$\frac{q\mathbf{E}}{\hbar}\cdot\nabla_{\mathbf{k}}f_\lambda = -\sum_{\lambda'}\Theta_{\lambda\lambda'}\Delta f_{\lambda'}, \tag{1}$$

where $q$ is the carrier charge, $\mathbf{E}$ is the electric field vector, $f_\lambda$ is the carrier occupation function indexed by $\lambda$ which represents the combined indices of band $n$ and wave vector $\mathbf{k}$, and $\Delta f_\lambda$ represents the deviation from equilibrium as $\Delta f_\lambda = f_\lambda - f_\lambda^0$ where $f_\lambda^0$ is the Fermi-Dirac distribution at a specified lattice temperature and chemical potential. $\Theta_{\lambda\lambda'}$ is the linearized collision integral as given by Eq. (3) of Ref. [21]. The collision integral depends on the phonon populations which may be perturbed by carrier scattering, but owing to the small free-carrier densities in the relevant experiments ($\lesssim 10^{14}\,\mathrm{cm}^{-3}$), this effect may be neglected here [17].

Equation (1) can be expressed as a linear system of equations using the linearized collision integral and a finite difference approximation for the reciprocal space gradient, as described in Sec. II A of Ref. [21]. The only modification to the governing equations in the present work is a change of sign for the reciprocal-space gradient to account for the charge carriers being holes. The BTE then takes the form

$$\sum_{\lambda'}\Lambda_{\lambda\lambda'}\Delta f_{\lambda'} = \sum_\gamma \frac{e\mathrm{E}_\gamma}{k_BT}v_{\lambda,\gamma}f_\lambda^0, \tag{2}$$

where $\mathrm{E}_\gamma$ and $v_{\lambda,\gamma}$ are the electric field strength and hole velocity in the $\gamma$ Cartesian axis, $k_B$ is the Boltzmann constant, and $T$ is the lattice temperature. The relaxation operator $\Lambda_{\lambda\lambda'}$ is defined as

$$\Lambda_{\lambda\lambda'} = \Theta_{\lambda\lambda'} - \sum_\gamma \frac{e\mathrm{E}_\gamma}{\hbar}D_{\lambda\lambda',\gamma}, \tag{3}$$

where $D_{\lambda\lambda',\gamma}$ is the finite -difference matrix (FDM) approximating the $\gamma$-axis component of the reciprocal-space gradient. The solution to the linear system, $\Delta f_\lambda$, can be used to calculate various observables including the mobility and PSD. The mobility is given as [29]

$$\mu_{\alpha\beta}(\mathbf{E}) = \frac{2e^2}{k_BT\mathcal{V}}\sum_\lambda v_{\lambda,\alpha}\sum_{\lambda'}\Lambda^{-1}_{\lambda\lambda'}(v_{\lambda',\beta}f^0_{\lambda'}), \tag{4}$$

where $\mathcal{V}$ is the supercell volume, $\alpha$ is the direction along which the current is measured, and $\beta$ is the direction along which the electric field is applied. The PSD is given as

$$S_{j_\alpha j_\beta}(\mathbf{E},\omega) = 2\left(\frac{2e}{\mathcal{V}}\right)^2 \times \Re\left[\sum_\lambda v_{\lambda,\alpha}\sum_{\lambda'}(i\omega\mathbb{I}+\Lambda)^{-1}_{\lambda\lambda'}(f^s_{\lambda'}(v_{\lambda',\beta}-V_\beta))\right], \tag{5}$$

where $\omega$ is the angular frequency, $\mathbb{I}$ is the identity matrix, and $f_\lambda^s = f_\lambda^0 + \Delta f_\lambda$ is the steady distribution. Here, $V_\beta$ is the drift velocity, given by

$$V_\beta = \frac{1}{N}\sum_\lambda v_{\lambda,\beta}f_\lambda^s, \tag{6}$$

where $N = \sum_\lambda f_\lambda$ is the number of holes in the Brillouin zone. Further details are available in Sec. II B of Ref. [21].

### B. Finite-difference matrix

Within the Monkhorst-Pack Brillouin zone discretization scheme used here [30], the reciprocal-space gradient may be approximated by an FDM as defined by Eqs. (8) and (B2) of Refs. [31,32], respectively. In prior high-field works [11,12,21,22], the inclusion of only first-nearest neighbors provided adequate accuracy at $T \geqslant 77$ K. At temperatures below 77 K, we found the quality of this numerical finite difference approximation to be poor. This issue could, in principle, be addressed by increasing the grid density. However, for $T < 77$ K the grid density cannot be made sufficiently large to achieve the needed accuracy due to computational limitations.

Instead, we utilize the same prior FDM method but use multiple shells for the finite difference approximation, as originally proposed in Ref. [32]. To determine the shell weights, an analytical method cannot be used since the combination of a body-centered cubic Monkhorst-Pack mesh for Si and the use of multiple shells leaves low-order mixed partial derivatives which cannot be eliminated using a finite number of shells. To overcome this limitation, we solve for shell weights for a selected electronic band by the minimization of an objective function measuring the difference between exact and approximate derivatives

$$\mathrm{Error}(T,\{w_b\}) = \frac{\sum_\lambda\left(\left[\frac{\partial f_\lambda^0}{\partial k_\gamma}\right] - [D_\gamma(\{w_b\})\,f_\lambda^0]\right)^2 f_\lambda^0}{\sum_\lambda\left[\frac{\partial f_\lambda^0}{\partial k_\gamma}\right]^2 f_\lambda^0}, \tag{7}$$

where $[\frac{\partial f_\lambda^0}{\partial k_\gamma}]$ is the analytical derivative of the Fermi-Dirac function $f_\lambda^0$ and $D_\gamma(\{w_b\})$ is the FDM representation of a single $\gamma$-axis component of the reciprocal-space gradient. The temperature dependence of the objective function arises from the temperature dependence of $f_\lambda^0$. The FDM is defined using $\{w_b\}$, which is the set of shell weights and are the minimization parameters, subject to the constraint $\sum_b w_b = 1$. The subscript $b$ identifies the nearest-neighbor shell. We define the total number of shells in a scheme by $B$.

TABLE I. Calculated FDM shell weights $w_b$ using Eq. (7) and $T = 77$ K for various numbers of shells $B$.

| | Shell ($b$) | | | | | | |
|---|---|---|---|---|---|---|---|
| Total shells ($B$) | 1 | 2 | 3 | 4 | 5 | 6 | 7 |
| 1 | 1.000 | | | | | | |
| 2 | 0.725 | 0.275 | | | | | |
| 3 | 1.390 | 0.530 | −0.920 | | | | |
| 4 | 1.270 | 0.600 | −0.490 | −0.380 | | | |
| 5 | 1.280 | 0.590 | −0.480 | −0.370 | −0.020 | | |
| 6 | 1.310 | 0.590 | −0.420 | −0.680 | 0.030 | 0.170 | |
| 7 | 1.380 | 0.730 | −0.330 | −0.980 | −0.450 | 0.100 | 0.550 |

It was found that relative to the one-shell case ($B = 1$) at $T \leqslant 77$ K, the error defined by Eq. (7) decreased by 96% with the inclusion of three shells ($B = 3$), and by a further 77% with seven shells ($B = 7$). In terms of transport properties, we compare the high-field dc mobility in different cases via RMS difference (defined as $||y_1 - y_2||_2 \, / \, ||y_1||_2$, where $y$ is the property of interest). The mobility obtained using $B = 3$ and $B = 7$ agreed with the $B = 1$ case to within 2.1% even at 20 K and up to 10 kVcm$^{-1}$. The RMS difference between $B = 3$ and $B = 7$ was 0.3%. This agreement indicates that, despite being optimized to accurately calculate the gradient of the Fermi-Dirac function $f_\lambda^0$, the higher-order FDM still provides an accurate result when applied to the hot-carrier distribution function $f_\lambda$.

For noise properties, however, $B \geqslant 3$ was found to be necessary to remove numerical artifacts. Therefore, we used $B = 3$ at 77 K and $B = 7$ for $T < 77$ K. For points near the edge of the defined grid for which the default number of shells ($B$) is not possible, we used the maximum number of shells with fully defined neighboring points. For uniformity, the shell weights were calculated using $T = 77$ K, as temperature had only a negligible effect on $\{w_b\}$. For example, calculating $\{w_b\}$ for $B = 7$ at $T = 20$ K results in an RMS difference in the 20 K drift velocities of only 3.7% compared to calculations using shell weights optimized at 77 K. Shell weights $w_b$ for each value of $b$ and $B$ are as shown in Table I.

### C. Numerical details

Band structure and phonon calculations were performed in QUANTUM ESPRESSO [33] as in Ref. [22]. Fine-grid interpolation and scattering rate calculations were performed via PERTURBO [34]. A $250^3$ ($250 \times 250 \times 250$) grid with 2.5 meV Gaussian smearing was used for $T > 6$ K, and a $325^3$ grid with 1.25 meV smearing was used for $T = 6$ K. Increasing the Gaussian width to 1.55 meV at 6 K resulted in a maximum change in drift velocity of 1.7% at any field. The energy windows for scattering rate calculations were 80 and 57 meV for $T > 6$ K and $T = 6$ K, respectively. Increasing the energy window to 90 meV at 77 K and a grid of $180^3$ resulted in a 3% difference at the maximum field studied (10 kVcm$^{-1}$), and increasing the window to 70 meV at 6 K and a grid of $200^3$ resulted in a similar 3.5% difference at 0.84 kVcm$^{-1}$. The linearized Boltzmann transport equation [21] was then solved via the GMRES algorithm [35] to calculate the steady-state distribution function, mobility, and noise quantities [21,22]. Only the heavy holes were included to reduce computational costs; it was found that at 77 K omitting the light hole band resulted in an RMS difference of only 1.5% compared to results with both the heavy and light holes, and this error decreases with decreasing temperature owing to the decreasing occupation of the light and split-off bands.

## III. RESULTS

### A. Drift velocity

We first investigate the drift velocity characteristics of $p$-Si. The calculated drift velocity-field curves at various cryogenic temperatures are shown in Fig. 1. We observe that the *ab initio* calculations predict the two regimes of velocity saturation that are observed experimentally. The good agreement when only considering electron-phonon scattering indicates that ionized impurity scattering is negligible in these high-purity samples ($\gtrsim$100 kΩ cm) even at cryogenic temperatures, as originally concluded in the experimental studies

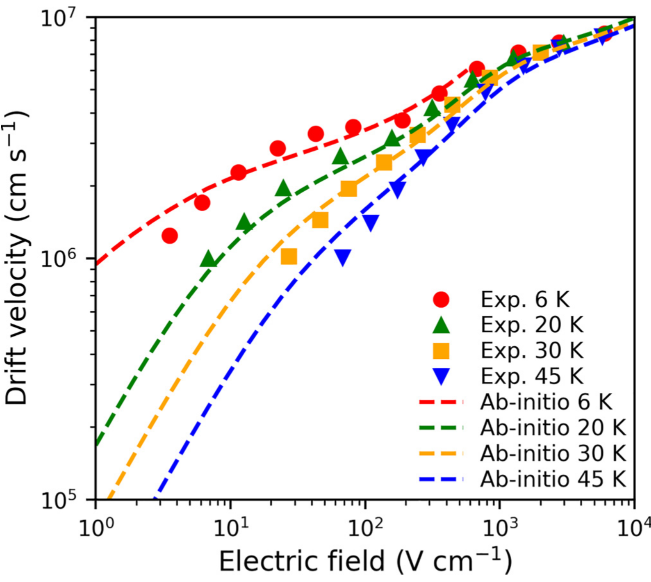


FIG. 1. Hole drift velocity versus electric field in the [100] direction. Experimental values from Ref. [17] (6 K as red circles, 20 K as green upward triangles, 30 K as yellow squares, 45 K as blue downward triangles). Calculated values also shown (dashed lines with identical color scheme to experiment).

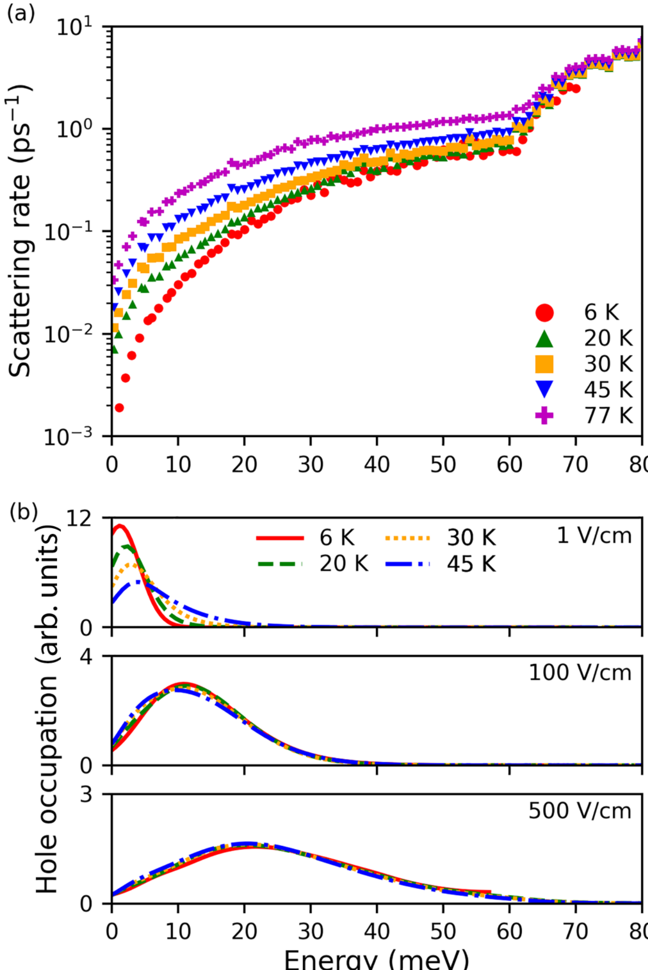


FIG. 2. (a) Calculated hole-phonon scattering rate versus energy from the valence band maximum at temperatures of 6 K (red circles), 20 K (green upward triangles), 30 K (yellow squares), 45 K (blue downward triangles), and 77 K (magenta crosses). (b) Hole occupation function versus energy from the valence band maximum at various electric fields applied in the [100] direction. The occupation is obtained using a kernel density estimate. Colors correspond to the same lattice temperatures as in (a). Data at 6 K are shown up to the 57 meV energy window at that temperature.

[17,18]. At $\lesssim$ 10 Vcm$^{-1}$, the drift velocity increases linearly with field following the Ohmic trend, followed by an increase with lesser slope from 10–200 Vcm$^{-1}$corresponding to the anomalous saturation regime. At ~200 Vcm$^{-1}$, the drift velocity increases further with nearly the same slope as in the Ohmic regime, but eventually enters another saturation regime at ~500 Vcm$^{-1}$. Near-quantitative agreement with experiment is achieved to within 8% (RMS) over all temperatures.

To gain insight into the origin of the low-field saturation regime, we show the calculated hole-phonon scattering rates versus energy in Fig. 2(a). In the following discussion, we focus only on the 20 K case for simplicity. At this temperature, we observe that the scattering rates increase rapidly with increasing energy; from hole energies of 0 to 20 meV there is an increase in scattering rates by a factor exceeding 200. However, from 20 to 60 meV the rates are relatively constant, only rising by a factor of 4. Above 60 meV optical phonon emission becomes possible and the scattering rates again rapidly rise with energy.

These differing trends below and above ~20 meV arise due to two factors. First, below ~40 K, the population of zone-edge acoustic phonons, which have the largest density of states among acoustic phonons, rapidly diminishes with temperature. Consequently, the acoustic phonon absorption rate approaches zero with decreasing temperature while the acoustic phonon emission rate approaches a constant, which causes a large disparity in scattering rates between low and high energies where absorption and emission are dominant, respectively. Second, the phonon density of states, which increases quadratically with energy up to a maximum at ~20 meV [36], causes a corresponding increase in scattering rates with energy from 0–20 meV. These factors together result in an strongly temperature-dependent increase in scattering rates from 0 to ~20 meV and relatively constant rates at higher energies up to ~60 meV.

We next examine the occupation function at various fields to establish which hole energies and corresponding scattering rates are relevant when the saturation feature occurs. We plot the hole occupation function versus energy and applied electric field in Fig. 2(b). At 1 Vcm$^{-1}$, we observe that nearly all holes are confined to energies less than 10 meV, and the hole occupation exhibits a clear dependence on temperature. For sufficiently strong electric fields ($\gtrsim$10 Vcm$^{-1}$), the weight of the distribution shifts towards 10–30 meV as shown in Fig. 2(b) at 100 Vcm$^{-1}$, where the slope of drift velocity with field reaches a local minimum. In this energy range, we observe the rapid increase in scattering rates with increase in energy due to zone-edge acoustic phonon emission. At 500 Vcm$^{-1}$, shown also in Fig. 2(b), the hole distribution has weight in the 30–60 meV region, where scattering rates are relatively constant. Above 500 Vcm$^{-1}$, some holes have energy exceeding ~60 meV and may undergo optical phonon emission processes.

We may now explain the relationship between acoustic phonon scattering and the first regime of drift velocity saturation. At low fields ($\lesssim$ 10 Vcm$^{-1}$), the drift velocity is linear with field corresponding to the Ohmic regime, as holes are approximately in equilibrium with the lattice and the mean scattering rate remains independent of field, a trend which occurs at all temperatures. However, at cryogenic temperatures and high fields (~40–200 Vcm$^{-1}$), carrier heating shifts the occupation to energies where the scattering rates are 1–2 orders of magnitude larger than those relevant at low fields. The higher scattering rates at these energies more than compensates the higher band velocity, causing a decrease in mobility and the drift velocity saturation.

At higher fields, above ~200 Vcm$^{-1}$, the increasing band velocity with energy compensates the relatively smaller increase in scattering rates. Therefore, the saturation “shoulder” ends, and drift velocity again increases with increasing field. Finally, at about ~500 Vcm$^{-1}$, optical phonon emission begins and another regime of drift velocity saturation occurs. At higher temperatures $\gtrsim$77 K, the scattering rates below 20 meV do not show a pronounced increase, and therefore the anomalous saturation regime does not occur. From these

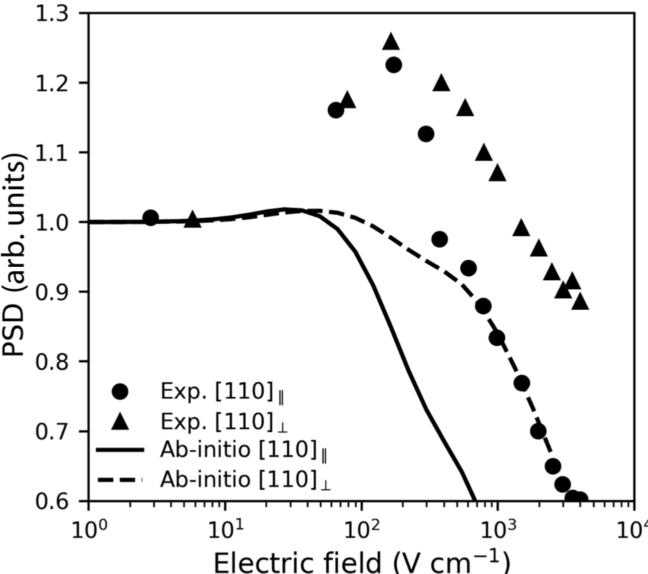


FIG. 3. PSD of current noise versus electric field applied in the [110] direction at 10 GHz. Experimental values from Ref. [27] (measurements taken parallel to [110] as circles, measurements taken in the transverse direction [$1\overline{1}0$] as upward triangles). Calculated data also shown [parallel (∥) as solid line, perpendicular (⊥) as dashed line].

findings, we may conclude that it is the energy-dependence of the acoustic phonon scattering rates at cryogenic temperatures which cause the saturation "shoulder" in $p$-Si between 10 and 200 $\mathrm{Vcm}^{-1}$for $T \lesssim 40$ K, in agreement with a prior work [23].

### B. Power spectral density

We now turn to the nonmonotonic trend of the microwave PSD versus electric field. This feature appears in the experimental 10 GHz PSD, which first increases and then decreases with an increasing electric field, leading to a peak at around 20 $\mathrm{Vcm}^{-1}$[26,27]. We have calculated the 10 GHz PSD for longitudinal and transverse measurement directions ([110] and [$1\overline{1}0$], respectively) versus [110] electric field strength, shown in Fig. 3. Normalized values are shown to facilitate the comparison of trends. The absolute PSD values would be uniformly overestimated by around 25% based on previous calculations of the mobility and diffusion coefficient and considering the Nyquist and Einstein relations linking the PSD, diffusion coefficient, and mobility at equilibrium [22]. The calculations do not agree quantitatively with experiment but show a qualitatively similar nonmonotonic trend. A firm conclusion regarding the origin of the discrepancy is difficult to draw owing to discrepancies between experimental reports (c.f. Fig. 1(b) of [26] and the various other experimental reports of the diffusion coefficient, namely Fig. 2(a) of Ref. [37] and Fig. 3 of Ref. [38]) and the fact that only one reference exists for this particular data set. In the following discussion, we therefore consider the qualitative experimental trends rather than focusing on quantitative agreement.

Previous studies have attributed the trend to the competition of carrier heating (increasing PSD) and decreasing relaxation time (decreasing PSD) [27], as well as the convective noise mechanism which is influenced by the field-dependent energy relaxation time [28]. However, each explanation has inconsistencies. Regarding the first explanation, we note that the 10 GHz PSD measurements by Ref. [26,27] were used to calculate the diffusion coefficient, which is valid only in the low-frequency limit [39] ($\omega\tau_m \ll 1$, where $\tau_m$ is the momentum relaxation time appearing in the Drude conductivity expression [40]). In this limit, an increase in transport properties with increasing electric field due to carrier heating would be expected in not just the PSD but also in dc quantities such as mobility. However, the hole mobility in Si is observed to decrease with increasing field. Therefore, this explanation is inconsistent with the observed trends of other transport properties. Regarding the second explanation, the convective noise mechanism only affects the longitudinal PSD, not the transverse PSD (see Sec. 7.2 of Ref. [28]). Because the PSD peak appears in both measurement directions, the convective mechanism cannot be responsible for the peak. Therefore, the underlying cause of the nonmonotonic PSD feature remains unclear.

To identify the origin of the peak, we calculated the PSD versus both electric field and frequency. The result is shown in Fig. 4(a). The longitudinal PSD calculation in Fig. 3 corresponds to a horizontal slice of this plot at 10 GHz. The location of the peak, given by the dotted line, is observed to depend on both electric field and frequency. Because the peak is observed in our calculations which include only the heavy-hole band, interband scattering may be ruled out. Additionally, the feature is also observed when optical phonons are omitted, eliminating carrier streaming noise as the origin (see Sec. 7.4 of Ref. [28]). Therefore, we conclude that the peak must arise from qualities of the hole and phonon dispersion and acoustic phonon scattering rates.

Knowing that the convective mechanism cannot be responsible for the PSD peak, and without any other mechanism by which energy relaxation may produce the feature, we take as a working hypothesis that the energy dependence of the momentum relaxation time leads to the trend. However, within the fully *ab initio* framework, testing this hypothesis is difficult. Therefore, we introduce a simplified model relating the PSD to $\tau_m(E)$. Assuming equipartition and neglecting anisotropy, the PSD takes the form [41]

$$S_j(\omega, E) = \frac{S_j(0, E)}{1 + (\omega\tau)^2}, \tag{8}$$

where $\tau$ represents a characteristic relaxation time of the system (for instance momentum, energy, or intervalley relaxation), and $E$ represents the electric field strength. A derivation of this expression, considering the constant relaxation time to be $\tau_m$, can be found in Secs. 3 and 7 of Ref. [28]. A simple although less rigorous derivation can be performed by combining the Nyquist current noise (Refs. [42,43], Eqs. (6) and (1), respectively) and Drude ac conductivity (Ref. [40], Eq. (1.29)) to yield Eq. (8), also neglecting the field dependence.

For our model, we assume a monoenergetic hole distribution characterized by a momentum relaxation time depending on electric field $\tau_m(E)$. For simplicity, we further approximate $S_j(0, E) \propto \tau_m(E)$ as the low-frequency PSD is directly

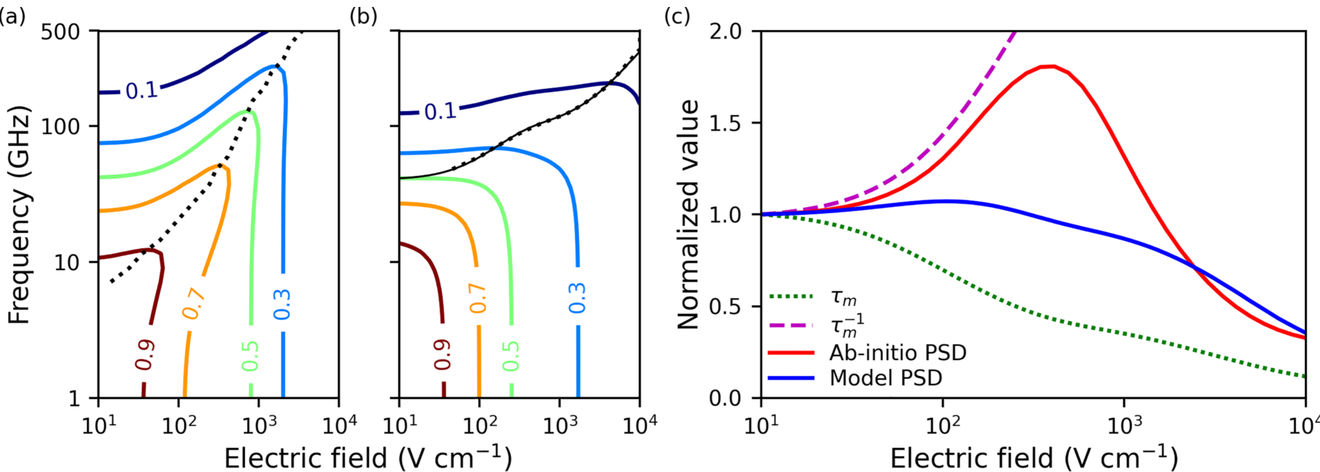


FIG. 4. (a) Contour map of normalized *ab initio* PSD of current fluctuations versus frequency and electric field. Location of peak in the horizontal slices (PSD vs field curves) also shown (dotted black line). (b) Contour map of normalized model PSD [Eq. (9)] versus frequency and electric field. An analogous peak feature is observed as the *ab initio* PSD. Location of peak in the horizontal slices shown (dotted black line), as well as $\omega\tau_m(E) = 1$ (solid black line). (c) *Ab initio* PSD vs electric field in (a) (solid red line) and modeled PSD in (b) (solid blue line) at 60 GHz. The normalized momentum relaxation time is shown (dotted green line) as well as its inverse (dashed magenta line). The normalization constant for $\tau_m(E)$ is 3.86 ps.

proportional to the momentum relaxation time through the fluctuation-diffusion [39] and Einstein [19] relationships. These assumptions yield

$$S_j(\omega, E) \propto \frac{\tau_m(E)}{1 + (\omega\tau_m(E))^2}. \quad (9)$$

Now, the Einstein relationship holds only in the low-field limit, but it remains approximately valid at fields where the carrier distribution is sufficiently close to the equilibrium one. In the present case, the mean carrier energy at 20 $\mathrm{Vcm^{-1}}$, where nonmonotonic behavior is apparent, is only 2.2% larger than the equilibrium value, so the error arising from the use of the Einstein relationship should be on the order of this difference ($\lesssim 10\%$). Therefore, it is expected that Eq. (9) provides a qualitatively accurate description of PSD behavior at the electric fields of interest.

To plot Eq. (9), an expression for $\tau_m(E)$ is needed. From our *ab initio* results, we calculated the momentum relaxation time at each electric field by fitting a Lorentzian to the frequency dependence of the transverse ac mobility with an identical functional form as in Eq. (9). The resulting function $\tau_m(E)$ is shown in normalized form in Fig. 4(c).

Using this function, we compute PSD versus frequency and electric field strength using Eq. (9). The result is given in Fig. 4(b). We observe a qualitatively similar "ridge" trend as seen in the *ab initio* PSD. Horizontal slices, which yield PSD versus field strength, taken at high frequencies, display a peak, the location of which follows the same trend as in Fig. 4(a). Within this model, the location of the peak corresponds to $\omega\tau_m(E) = 1$, providing evidence that the field dependence of the momentum relaxation time $\tau_m(E)$ is responsible for the nonmonotonic PSD trend.

This behavior can be understood by inspecting the relative magnitude of the numerator $\tau_m(E)$ and the denominator $1 + (\omega\tau_m(E))^2$, which represent carrier scattering and carrier inertia [44], respectively. At sufficiently high temperatures and low frequencies such that $\omega\tau_m(E) \ll 1$, the PSD is proportional to $\tau_m(E)$ and decreases with field due to $\tau_m(E)$ decreasing. However, when $\omega\tau_m(E) \gg 1$ is satisfied, which occurs at some combinations of sufficiently low temperatures, high frequencies, and low fields, then, with increasing field as $\tau_m(E)$ decreases the inertial term $1 + (\omega\tau_m(E))^2$ decreases faster than $\tau_m(E)$ itself. Thus, the PSD rises as $\mathrm{PSD}(\omega, E) \sim 1/\tau_m(E)$. Once $\omega\tau_m(E) \ll 1$ is satisfied again at high enough fields, which will occur regardless of temperature and frequency, the PSD again decreases with field. These different behaviors are displayed in Fig. 4(c), along with horizontal slices of Figs. 4(a) and 4(b) at 60 GHz. We have chosen this higher frequency for the plots to make the relevant features in the model more visible. We observe that at low fields, both the modeled and *ab initio* PSD exhibit the expected $\tau_m(E)^{-1}$ behavior, and the $\tau_m(E)$ behavior at high fields. These different trends enable a peak in the PSD, driven solely by the field dependence of the momentum relaxation time.

We now discuss why the *ab initio* PSD results display a peak even when $\omega\tau_m(E = 0) \gtrsim 1$ is not satisfied, a condition strictly necessary for a peak to appear in the model. In a real system, the hole distribution is not characterized by a single energy, as was assumed in the model. Therefore, although the momentum relaxation time $\tau_m(E)$ may satisfy $\omega\tau_m(E) \sim 1$, the lifetime of some states $\tau_\lambda = \Theta_{\lambda,\lambda}^{-1}$ may span a range of values of $\omega\tau_\lambda$. Therefore, even at frequencies where $\omega\tau_m(E = 0) < 1$, some electronic states for which $\omega\tau_\lambda \gg 1$ may have non-negligible occupation. The carriers in these states may then contribute to the occurrence of a nonmonotonic PSD trend, even at lower frequencies than are required to satisfy $\omega\tau_m(E = 0) \gtrsim 1$.

## IV. DISCUSSION

We now examine our findings in the context of prior works. The role of the field dependence of the momentum relaxation time in producing nonmonotonic trends of ac mobility with electric field has been previously reported [45]. Various

studies have incorporated field dependence into the momentum relaxation time of ac mobility models and observed different trends depending on the frequency. At low frequencies such that $\omega\tau_m(E=0) \ll 1$, the ac mobility is both theoretically predicted [46,47] and experimentally observed [48] to decrease monotonically with increasing electric field, as expected for systems with sublinear current-voltage characteristics. However, at frequencies such that $\omega\tau_m(E=0) \geqslant 1$, other studies predicted a nonmonotonic dependence of ac mobility on electric field [49,50].

Experimentally, nonmonotonic trends of ac mobility with electric field have been reported for *n*-InSb [45,51]. These experiments measured ac mobility at 77 K as a function of field from 0–165 $\mathrm{Vcm}^{-1}$and from 0–83.7 GHz, which includes the case $\omega\tau_m(E=0) \approx 1$. The measurements show nonmonotonic behavior when $\omega\tau_m(E=0) > 1$, with an initial rise in the ac mobility at low fields ($\lesssim 50$ $\mathrm{Vcm}^{-1}$), in contrast to the decreasing trend at lower frequencies. Furthermore, the data agree qualitatively with a hydrodynamic model [51] which predicts nonmonotonicity in the high-field ac mobility for frequencies above ∼50 GHz. Since the ac mobility is proportional to the PSD at low electric fields through the Nyquist relationship, these prior findings are consistent with our conclusions. On the other hand, prior studies of the microwave PSD concluded the nonmonotonic trend was due to a competition between carrier heating and decreasing relaxation time with increasing field [27], and convective noise [28]. However, our study and prior ac mobility studies support that the field dependence of the momentum relaxation time alone as the origin.

## V. SUMMARY

We have investigated the origin of anomalous high-field transport and noise characteristics in *p*-Si at cryogenic temperatures using a modified high-field formalism for *ab initio* charge transport. We find that the additional regime of drift velocity saturation that occurs for $T < 40$ K is due to acoustic phonon emission, in agreement with a prior work. We also find that the peak in the power spectral density of current fluctuations which occurs at 77 K and 10 GHz is due to the field dependence of the momentum relaxation time, contrary to the conclusions of prior studies. This work highlights the capabilities of the *ab initio* method for providing microscopic insight into high-field transport and noise phenomena in semiconductors.

## ACKNOWLEDGMENT

This work was supported by the National Science Foundation under Award No. 1911926.


[1] M. Lundstrom, *Fundamentals of Carrier Transport*, 2nd ed. (Cambridge University Press, Cambridge, UK, 2000).

[2] D. Ferry, *Semiconductor Transport* (CRC Press, Boca Raton, FL, 2000).

[3] S. Poncé, W. Li, S. Reichardt, and F. Giustino, Rep. Prog. Phys. **83**, 036501 (2020).

[4] M. Bernardi, Eur. Phys. J. B **89**, 239 (2016).

[5] F. Giustino, Rev. Mod. Phys. **89**, 015003 (2017).

[6] C. Jacoboni and P. Lugli, *The Monte Carlo Method for Semiconductor Device Simulation*, 1st ed. (Springer, New York, 1989).

[7] J. Mateos, T. Gonzalez, D. Pardo, V. Hoel, and A. Cappy, IEEE Trans. Electron Devices **47**, 1950 (2000).

[8] Edited by K. Hess, *Monte Carlo Device Simulation: Full Band and Beyond*, The Springer International Series in Engineering and Computer Science Vol. 144 (Springer Science + Business Media, LLC, 1991).

[9] C. Jungemann, S. Keith, M. Bartels, and B. Meinerzhagen, IEICE Transactions on Electronics **E82-C**, 870 (1999).

[10] N.-E. Lee, J.-J. Zhou, H.-Y. Chen, and M. Bernardi, Nat. Commun. **11**, 1607 (2020).

[11] P. S. Cheng, J. Sun, S.-N. Sun, A. Y. Choi, and A. J. Minnich, Phys. Rev. B **106**, 245201 (2022).

[12] B. Hatanpää, A. Y. Choi, P. S. Cheng, and A. J. Minnich, Phys. Rev. B **107**, L041110 (2023).

[13] T.-H. Liu, B. Song, L. Meroueh, Z. Ding, Q. Song, J. Zhou, M. Li, and G. Chen, Phys. Rev. B **98**, 081203(R) (2018).

[14] J. Shin, G. A. Gamage, Z. Ding, K. Chen, F. Tian, X. Qian, J. Zhou, H. Lee, J. Zhou, L. Shi, T. Nguyen, F. Han, M. Li, D. Broido, A. Schmidt, Z. Ren, and G. Chen, Science **377**, 437 (2022).

[15] S. Yue, F. Tian, X. Sui, M. Mohebinia, X. Wu, T. Tong, Z. Wang, B. Wu, Q. Zhang, Z. Ren, J. Bao, and X. Liu, Science **377**, 433 (2022).

[16] C. Jacoboni and L. Reggiani, Adv. Phys. **28**, 493 (1979).

[17] G. Ottaviani, L. Reggiani, C. Canali, F. Nava, and A. Alberigi-Quaranta, Phys. Rev. B **12**, 3318 (1975).

[18] C. Canali, C. Jacoboni, F. Nava, G. Ottaviani, and A. Alberigi-Quaranta, Phys. Rev. B **12**, 2265 (1975).

[19] L. Reggiani, General theory, in *Hot-Electron Transport in Semiconductors*, edited by L. Reggiani (Springer, Berlin, Heidelberg, 1985), pp. 7–86.

[20] J. P. Nougier, in *Physics of Nonlinear Transport in Semiconductors*, NATO Advanced Study Institutes Series: Series B, Physics, Vol. 52, edited by D. K. Ferry, J. R. Barker, and C. Jacoboni (Plenum Press, New York, 1980), pp. 415–465.

[21] A. Y. Choi, P. S. Cheng, B. Hatanpää, and A. J. Minnich, Phys. Rev. Mater. **5**, 044603 (2021).

[22] D. S. Catherall and A. J. Minnich, Phys. Rev. B **107**, 035201 (2023).

[23] J. Von Borzeszkowski, Physica Status Solidi B **73**, 607 (1976).

[24] Y. Ohno, J. Appl. Phys. **64**, 4549 (1988).

[25] B. Fischer and K. R. Hofmann, Appl. Phys. Lett. **76**, 583 (2000).

[26] V. Bareikis, R. Barkauskas, A. Galdikas, and R. Katilius, Sov. Phys. Semicond. **14**, 1046 (1980).

[27] V. Bareikis, A. Galdikas, and R. Miliusyte, in *Hot Electron Diffusion / Diffuziia goriachikh elektronov*, Electrons in Semiconductors / Elektrony v poluprovodnikakh Vol. 3 (Vilnius: Mokslas, 1981), Chap. 4, pp. 127–161, academy of Sciences of the Lithuanian SSR / Lietuvos TSR Moksly Akademija.

[28] H. L. Hartnagel, R. Katilius, and A. Matulionis, *Microwave Noise in Semiconductor Devices* (John Wiley & Sons, Inc., New York, 2001).
[29] W. Li, Phys. Rev. B **92**, 075405 (2015).
[30] H. J. Monkhorst and J. D. Pack, Phys. Rev. B **13**, 5188 (1976).
[31] A. A. Mostofi, J. R. Yates, Y.-S. Lee, I. Souza, D. Vanderbilt, and N. Marzari, Comput. Phys. Commun. **178**, 685 (2008).
[32] N. Marzari and D. Vanderbilt, Phys. Rev. B **56**, 12847 (1997).
[33] P. Giannozzi, S. Baroni, N. Bonini, M. Calandra, R. Car, C. Cavazzoni, D. Ceresoli, G. L. Chiarotti, M. Cococcioni, I. Dabo, A. D. Corso, S. de Gironcoli, S. Fabris, G. Fratesi, R. Gebauer, U. Gerstmann, C. Gougoussis, A. Kokalj, M. Lazzeri, L. Martin-Samos *et al.*, J. Phys.: Condens. Matter **21**, 395502 (2009).
[34] J.-J. Zhou, J. Park, I.-T. Lu, I. Maliyov, X. Tong, and M. Bernardi, Comput. Phys. Commun. **264**, 107970 (2021).
[35] P. Virtanen, R. Gommers, T. E. Oliphant, M. Haberland, T. Reddy, D. Cournapeau, E. Burovski, P. Peterson, W. Weckesser, J. Bright, S. J. van der Walt, M. Brett, J. Wilson, K. J. Millman, N. Mayorov, A. R. J. Nelson, E. Jones, R. Kern, E. Larson, C. J. Carey *et al.*, Nature Methods **17**, 261 (2020).
[36] D. S. Kim, H. L. Smith, J. L. Niedziela, C. W. Li, D. L. Abernathy, and B. Fultz, Phys. Rev. B **91**, 014307 (2015).
[37] L. Reggiani, J. Phys. Soc. Jpn. Suppl. A **49**, 317 (1980), proc. 15th Int. Conf. Physics of Semiconductors.
[38] D. Gasquet, B. Azais, J. C. Vaissiere, and J. P. Nougier, in *Noise in Physical Systems and 1/f Noise - 1985*, edited by A. d'Amico and P. Mazzetti (Elsevier, Amsterdam, Netherlands, 1986), pp. 231–233.
[39] S. V. Gantsevich, V. L. Gurevich, and R. Katilius, Riv. del Nuovo Cim. **2**, 1 (1979).
[40] N. W. Ashcroft and N. D. Mermin, *Solid State Phyiscs*, 1st ed. (Saunders College Publishing, Philadelphia, PA, 1976).
[41] Y. K. Pozhela, Transport parameters from microwave conductivity and noise measurements, in *Hot-Electron Transport in Semiconductors*, edited by L. Reggiani (Springer, Berlin, Heidelberg, 1985), pp. 113–147.
[42] H. Nyquist, Phys. Rev. **32**, 110 (1928).
[43] J. B. Johnson, Phys. Rev. **32**, 97 (1928).
[44] K. Champlin, D. Armstrong, and P. Gunderson, Proc. IEEE **52**, 677 (1964).
[45] E. Bonek, J. Appl. Phys. **43**, 5101 (1972).
[46] A. Gibson, J. Granville, and E. Paige, J. Phys. Chem. Solids **19**, 198 (1961).
[47] B. V. Paranjape, Phys. Rev. **122**, 1372 (1961).
[48] G. H. Glover, J. Appl. Phys. **44**, 1295 (1973).
[49] D. Mukhopadhyay and B. Nag, Electron. Lett. **5**, 20 (1969).
[50] K. Seeger and H. Pötzl, in *The Boltzmann Equation*, edited by E. G. D. Cohen and W. Thirring (Springer Vienna, Vienna, 1973), pp. 341–378.
[51] E. Bonek, H. Pötzl, and K. Richter, J. Phys. Chem. Solids **31**, 1151 (1970).